Optimized M2L Kernels for the Chebyshev Interpolation based Fast Multipole Method

Matthias Messner, Bérenger Bramas, Olivier Coulaud, Eric Darve

Optimized M2L Kernels for the Chebyshev Interpolation based Fast Multipole Method

Matthias Messner, Berenger Bramas, Olivier Coulaud, Eric Darve

October 27, 2012

Abstract

A fast multipole method (FMM) for asymptotically smooth kernel functions ($1/r$, $1/r^4$, Gauss and Stokes kernels, radial basis functions, etc.) based on a Chebyshev interpolation scheme has been introduced in [5]. The method has been extended to oscillatory kernels (eg. Helmholtz kernel) in [12]. Beside its generality this FMM turned out to be favorable due to its easy implementation and performance based on intense use of highly optimized BLAS libraries. However, a bottleneck has been the precomputation of the M2L operator and its higher computational intensity compared to other FMM formulations. Here, we present several optimizations for that operator, which is known to be the most costly FMM operator. The most efficient ones do not only reduce the precomputation time by a factor of more than 1000 but they also speed up the matrix-vector product. We conclude with comparisons and numerical validations of all presented optimizations.

1 Introduction

Since the invention of the fast multipole method (FMM) in [7] extensive research has been done on this algorithm; the FMM reduces the cost of the matrix-vector product from $\mathcal{O}(N^2)$ to $\mathcal{O}(N)$ or $\mathcal{O}(N \log N)$ depending on the underlying kernel function. Most FMM variants have been developed and optimized for specific kernel functions [13, 8, 3, 2]. However, some have also been formulated so the FMM is independent of the kernel function [14, 10, 6, 5, 12]. The paper at hand addresses the optimization of one of these formulations, the so called black-box FMM (bbFMM) presented in [5]. It is based on the approximation of the kernel function via a Chebyshev interpolation and is a black-box scheme for kernel functions that are asymptotically smooth, e.g., $1/r^n$ with $r = |x - y|$ and $n \in \mathbb{N}$. The bbFMM has been extended to the directional FMM (dFMM) for oscillatory kernels in [12]. It is suitable for any kernel function of the type $g(r)e^{\imath kr}$ where $g(r)$ is an asymptotically smooth function ($\imath^2 = -1$ is the imaginary unit and k the wavenumber).

The main idea of the FMM is to properly separate near-field ($|x-y| \to 0$) and far-field ($|x-y| \to \infty$). The near-field is evaluated directly and the far-field can be approximated and thus computed efficiently. In the usual notation the operators involved in near-field computations are the P2P and in far-field computations the P2M, M2M, M2L, L2L and L2P. It is well known that the M2L operator is the costliest one. In this paper we focus on various optimizations of this operator for both, the bbFMM and the dFMM. First, we address the optimization proposed in [5, 12]. One of its weaknesses is that many M2L operators end up having suboptimal low-rank representations and that affects the runtime negatively. A further recompression leads to optimal low-rank representations. However, the main bottleneck, the expensive precomputation of the M2L operators, is not tackled yet. We introduce a new set of optimizations whose idea is to exploit symmetries in the arrangement of the M2L operators. This allows us to express all M2L operators as permutations of a subset only. Besides drastically reducing precomputation time and memory requirement this approach paves also the road for blocking schemes (use of highly optimized matrix-matrix product implementations due to better cache reuse). We focus on performance and on reducing the precomputation time. Both are important factors for the FMM: the precomputation time is crucial if we are interested

in only one matrix-vector product, however, if we are interested in many matrix-vector products (iterative solution of linear systems) the runtime, depending on the cost of applying an M2L operator, becomes more and more dominant.

The paper is organized as follows. In Sec. 2 we briefly recall the bbFMM and the dFMM and introduce notations we need for explanations later in this paper. In Sec. 3 we address the separation of near- and far-field, we introduce the notion of transfer vector to uniquely identify M2L operators and speak about the dependency of interactions lists on the underlying kernel function. We start Sec. 4 with a brief recall of the known optimization of the M2L operator and suggest further improvements. Then, we present the new set of optimizations and explain them in details. Finally, in Sec. 5 we present numerical results. We compare all variants for bbFMM and dFMM and point out strengths and weaknesses of all variants.

2 Pairwise particle interactions

The problem statement reads as follows. Assume, the cells X and Y contain source $\{y_j\}_{j=1}^N$ and target particles $\{x_i\}_{i=1}^M$, respectively. Compute the interactions

$$f_i = \sum_{j=1}^{N} K(x_i, y_j) w_j \quad \text{for } i, \dots, M. \tag{1}$$

The kernel function $K(x, y)$ describes the influence of the source particles onto the target particles. The cost of directly evaluating the summation in Eqn. (1) grows like $\mathcal{O}(MN)$ which becomes prohibitive as $M, N \to \infty$ and it is why we need a fast summation scheme.

2.1 Fast summation schemes based on Chebyshev interpolation

For a detailed derivation and error analysis of the FMM based on Chebyshev interpolation we refer the reader to [5, 12]. We adapt most of their notations and repeat only concepts which are necessary to understand explanations hereafter.

Let the function $f : \mathbb{R}^3 \to \mathbb{C}$ be approximated by a Chebyshev interpolation scheme as

$$f(x) \sim \sum_{|\alpha| \le 3\ell} S_\ell(x, \bar{x}_\alpha) f(\bar{x}_\alpha) \tag{2}$$

with the 3-dimensional multi-index $\alpha = (\alpha_1, \alpha_2, \alpha_3)$ and $|\alpha| = \max(\alpha_1, \alpha_2, \alpha_3)$ with $\alpha_i \in (1, \dots, \ell)$. The interpolation points $\bar{x}_\alpha = (\bar{x}_{\alpha_1}, \bar{x}_{\alpha_2}, \bar{x}_{\alpha_3})$ are given by the tensor-product of the Chebyshev roots $\bar{x}_{\alpha_i}$ of the Chebyshev polynomial of first kind $T_\ell(x) = \cos(\arccos x)$ with $x \in [-1, 1]$. The interpolation operator reads as

$$S_\ell(x, \bar{x}_\alpha) = S_\ell(x_1, \bar{x}_{\alpha_1})\, S_\ell(x_2, \bar{x}_{\alpha_2})\, S_\ell(x_3, \bar{x}_{\alpha_3}). \tag{3}$$

For interpolation on arbitrary intervals, we need the affine mapping $\Phi : [-1, 1] \to [a, b]$. We omit it hereafter for the sake of readability.

2.1.1 Black–box FMM (bbFMM)

If two cells X and Y are well separated, we know from [5] that *asymptotically smooth kernel functions* can be interpolated as

$$K(x, y) \sim \sum_{|\alpha| \le \ell} S_\ell(x, \bar{x}_\alpha) \sum_{|\beta| \le \ell} K(\bar{x}_\alpha, \bar{y}_\beta)\, S_\ell(y, \bar{y}_\beta). \tag{4}$$

We insert the above approximation into Eqn. (1) and obtain

$$f_i \sim \sum_{|\alpha| \le \ell} S_\ell(x_i, \bar{x}_\alpha) \sum_{|\beta| \le \ell} K(\bar{x}_\alpha, \bar{y}_\beta) \sum_{j=1}^{N} S_\ell(y_j, \bar{y}_\beta)\, w_j \tag{5}$$

which we split up in a three-stage fast summation scheme.

1. Particle to moment (P2M) or moment to moment (M2M) operator: equivalent source values are anterpolated at the interpolation points $\bar{y}_\beta \in Y$ by

$$W_\beta = \sum_{j=1}^{N} S(y_j, \bar{y}_\beta)\, w_j \quad \text{for} \quad |\beta| \leq \ell. \tag{6}$$

2. Moment to local operator (M2L): target values are evaluated at the interpolation points $\bar{x}_\alpha \in X$ by

$$F_\alpha = \sum_{|\beta|\leq\ell} K(\bar{x}_\alpha, \bar{y}_\beta)\, W_\beta \quad \text{for} \quad |\alpha| \leq \ell. \tag{7}$$

3. Local to local (L2L) or local to particle (L2P) operator: target values are interpolated at final points $x_i \in X$ by

$$f_i \sim \sum_{|\alpha|\leq\ell} S(x_i, \bar{x}_\alpha)\, F_\alpha \quad \text{for} \quad i = 1, \ldots, M. \tag{8}$$

Recall, the cells X and Y are well separated and thus all contributions of f_i can be computed via the above presented fast summation scheme (no direct summation is necessary).

2.1.2 Directional FMM (dFMM)

Whenever we deal with *oscillatory kernel functions*, e.g., the Helmholtz kernel, the wavenumber k comes into play. Depending on the diameter of the cells X and Y and the wavenumber they are either in the low-frequency or in the high-frequency regime. In the low-frequency regime the fast summation schemes of the dFMM and the bbFMM do not differ. In the high-frequency regime the fast summation scheme needs to become directional. From [12] we know that any oscillatory kernel function $K(x,y) = G(x,y)e^{\imath k|x-y|}$, where $G(x,y)$ is an asymptotically smooth function, can be rewritten as

$$K(x,y) = K^u(x,y)e^{\imath ku\cdot(x-y)} \quad \text{with} \quad K^u(x,y) = G(x,y)e^{\imath k(|x-y|-u\cdot(x-y))}. \tag{9}$$

We assume that the cells X and Y of width w are centered at c_x and c_y and c_y lies in a cone of direction u being centered at c_x (think of the domain around X being virtually subdivided in cones given by directional unit vectors $\{u_c\}_{c=1}^{C}$, where C is determined by their aperture). If the cell pair (X,Y) satisfies the *separation* criterion $\mathcal{O}(kw^2)$ and the *cone-aperture* criterion $\mathcal{O}(1/kw)$, the error of the Chebyshev interpolation of the kernel function $K^u(x,y)$ decays exponentially in the interpolation order ℓ (the error independent of the wavenumber k; see [11, 12]).

$$K^u(x,y) \sim \sum_{|\alpha|\leq\ell} S_\ell(x,\bar{x}_\alpha) \sum_{|\beta|\leq\ell} K^u(\bar{x}_\alpha,\bar{y}_\beta)\, S_\ell(y,\bar{y}_\beta). \tag{10}$$

We insert the above interpolated kernel function in Eqn. (1) and obtain

$$f_i \sim e^{\imath ku\cdot x_i} \sum_{|\alpha|\leq\ell} S_\ell(x_i,\bar{x}_\alpha)e^{-\imath ku\cdot\bar{x}_\alpha} \sum_{|\beta|\leq\ell} K(\bar{x}_\alpha,\bar{y}_\beta)e^{\imath ku\cdot\bar{y}_\beta} \sum_{j=1}^{N} S_\ell(y_j,\bar{y}_\beta)e^{-\imath ku\cdot y_j}\, w_j \tag{11}$$

for all $i = 1, \ldots, M$. Similarly as with the bbFMM, a three-stage fast summation scheme for oscillatory kernels in the high-frequency regime can be constructed.

1. Particle to moment (P2M) or moment to moment (M2M) operator: equivalent source values are anterpolated at the interpolation points $\bar{y}_\beta \in Y$ by

$$W_\beta^u = e^{\imath ku\cdot\bar{y}_\beta} \sum_{j=1}^{N} S(y_j,\bar{y}_\beta)\, e^{-\imath ku\cdot y_j}\, w_j \quad \text{for} \quad |\beta| \leq \ell. \tag{12}$$

2. Moment to local operator (M2L): target values are evaluated at the interpolation points $\bar{x}_\alpha \in X$ by

$$F^u_\alpha = \sum_{|\beta|\le\ell} K(\bar{x}_\alpha, \bar{y}_\beta)\, W^u_\beta \quad \text{for} \quad |\alpha| \le \ell. \tag{13}$$

3. Local to local (L2L) or local to particle (L2P) operator: target values are interpolated at final points $x_i \in X$ by

$$f_i \sim e^{\imath k u\cdot x_i} \sum_{|\alpha|\le\ell} S(x_i, \bar{x}_\alpha)\, e^{-\imath k u\cdot \bar{x}_\alpha}\, F^u_\alpha \quad \text{for} \quad i = 1, \dots, M. \tag{14}$$

Even though the bbFMM and the dFMM are here presented as single-level schemes they are usually implemented as multilevel schemes. Strictly speaking, the steps one and three of both schemes are the P2M and L2P operators. Let us recall briefly on the directional M2M and L2L operators of dFMM: based on the criterion $\mathcal{O}(1/kw)$, the aperture of the cones at the upper level is about half the aperture at the lower level. Due to a nested cone construction along octree levels, we are able to preserve the accuracy of the Chebyshev interpolation scheme. For a detailed description of all operators we refer to [5, 12])

Note, the similarity of the M2L operators (step two of both schemes) for the bbFMM and the dFMM. In fact, the only difference in their implementation is that in the bbFMM case we have one loop over all cell pairs, whereas in the dFMM case we have two loops: the outer loop over all existing cones of direction $\{u_c\}_{c=1}^{C}$ and the inner loop over all cell pairs lying in the current cone. Hereafter, we focus only on the M2L operators and efficient numerical schemes to apply them.

3 M2L operators

The first step of any FMM consists in a proper separation of near- and far-field. After that, the near-field is evaluated directly and the far-field efficiently using a fast summation scheme. In this section, we focus on the first step. The union of near- and far-field of a target cell X is spatially restricted to the near-field of its parent cell. Algorithm 1 explains how these interactions are computed for dFMM [12]. The recursive partitioning starts with the two root cells X and Y of the octrees for source and target particles. If a pair of cells satisfies the separation criterion in the high- or low-frequency regime, Y is a far-field interaction of X. Else, if they are at the leaf level of the octree, Y is a near-field interaction of X. If none is true, the cell is subdivided and the tests are repeated. In line 3 in Alg. 1 we use the term directional far-field, a concept

Algorithm 1 Separate near- and far-field in the low- and high-frequency regime

```
1:  function SeparateNearAndFarField(X, Y)
2:      if (X, Y) are admissible in the high-frequency regime then
3:          add Y to the directional far-field of X return
4:      else if (X, Y) are admissible in the low-frequency regime then
5:          add Y to the far-field of X return
6:      else if (X, Y) are leaves then
7:          add Y to the near-field of X return
8:      else
9:          for all X_child ∈ X and all Y_child ∈ Y do
10:             SeparateNearAndFarField(X_child, Y_child)
11:         end for
12:     end if
13: end function
```

explained in detail in [12]: In the high-frequency regime the far-field is subdivided into cones of direction u needed by the directional kernel function $K^u(x, y)$. Each source cell Y is assigned to a cone and there are as many directional far-fields as there are cones.

3.1 Transfer vectors

In order to address interactions uniquely we introduce transfer vectors $t = (t_1, t_2, t_3)$ with $t \in \mathbb{Z}^3$. They describe the relative positioning of two cells X and Y and are computed as $t = {}^{(c_x - c_y)}/_{w}$ where c_x and c_y denote the centers of the cells X and Y and w their width. In the following we use transfer vectors to uniquely identify the M2L operator that computes the interaction between a target cell X and a source cell Y. In matrix notation an M2L operator reads as K_t of size $\ell^3 \times \ell^3$ and the entries are computed as

$$(\mathsf{K}_t)_{m(\alpha)n(\beta)} = K(\bar{x}_\alpha, \bar{y}_\beta) \tag{15}$$

with the interpolation points $\bar{x}_\alpha \in X$ and $\bar{y}_\beta \in Y$. Bijective mappings

$$m, n : \{1, \ldots, \ell\} \times \{1, \ldots, \ell\} \times \{1, \ldots, \ell\} \to \{1, \ldots, \ell^3\} \tag{16}$$

with $m^{-1}(m(\alpha)) = \alpha$ and $n^{-1}(n(\beta)) = \beta$ provide unique indices to map back and forth between multi-indices of $\bar{x}_\alpha$ and $\bar{y}_\beta$ and rows and columns of K_t. We choose them to be $m(\alpha) = (\alpha_1 - 1) + (\alpha_2 - 1)\ell + (\alpha_3 - 1)\ell^2 + 1$ and same for $n(\beta)$.

3.2 Interaction lists

Very commonly fast multipole methods are used for translation invariant kernel functions $K(x, y) = K(x + v, y + v)$ for any $v \in \mathbb{R}^3$. Because of that and because of the regular arrangement of interpolation points $\bar{x}$ and $\bar{y}$ in uniform octrees it is sufficient to identify unique transfer vectors at each level of the octree and to compute the respective M2L operators. In the following we refer to such sets of unique transfer vectors as interaction lists $T \subset \mathbb{Z}^3$.

If we consider *asymptotically smooth kernel functions* the near-field is limited to transfer vectors satisfying $|t| \leq \sqrt{3}$; it leads to $3^3 = 27$ near-field interactions (see [5]). In a multi-level scheme, these 27 near-field interactions contain all $6^3 = 216$ near- and far-field interactions of its eight child-cells. Far-field interactions are given by transfer-vectors that satisfy $|t| > \sqrt{3}$. This leads to a maximum of $6^3 - 3^2 = 189$ interactions per cell and we end up with the usual overall complexity of $\mathcal{O}(N)$ of fast multipole methods for asymptotically smooth kernel functions. The union of all possible far-field interactions of the eight child cells gives $7^3 - 3^3 = 316$ interactions. That is also the largest possible number of different M2L operators have to be computed per octree level. Most asymptotically smooth kernel functions happen also to be homogeneous $K(\alpha r) = \alpha^n K(r)$ of degree n. In other words, if we scale the distance $r = |x - y|$ between source and target by a factor of α the resulting potential is scaled by α^n, where n is a constant that depends on the kernel function. The advantage of homogeneous kernel functions is that the M2L operators need to be precomputed only at one level and can simply be scaled and used on other levels. This affects the precomputation time and the required memory.

If we consider *oscillatory kernel functions* we need to distinguish between the low- and high-frequency regime [12]. The admissibility criteria in the low-frequency regime are the same as those for asymptotically smooth kernel functions. However, in the high-frequency regime the threshold distance between near-field and far-field is $\mathcal{O}(kw^2)$; nonetheless, as shown in [12] we end up with the usual complexity of $\mathcal{O}(N \log N)$ of fast multipole methods for oscillatory kernel functions. It depends on the wavenumber k (a property of the kernel function). Thus, the size of near- and far-field is not a priori known as it is in the case of asymptotically smooth kernel functions. Table 1 summarizes the number of near and far-field interactions to be computed depending on different kernel functions.

Table 1: Number of near- and far-field interactions depends on the kernel function

type of kernel function	cells in near-field	cells in far-field
smooth	≤ 27 per leaf	≤ 316 per level
smooth and homogeneous	≤ 27 per leaf	≤ 316 for all levels
oscillatory	depends on k	depends on k

4 Optimizing the M2L operators

In all fast multipole methods the M2L operator adds the largest contribution to the overall computational cost: for bbFMM it grows like $\mathcal{O}(N)$ and for dFMM like $\mathcal{O}(N \log N)$. In this section, we first briefly recall the optimization that was used up to now and suggest an improvement. Then, we present a new set of optimizations that exploit the symmetries in the arrangement of the M2L operators.

4.1 Single low-rank approximation (SA)

In the following we explain the basics of the optimization used in [5, 12] and we refer to it as the SA variant hereafter. The idea is based on the fact that all M2L operators K_t with $t \in T$ can be assembled as a single big matrix in two ways: either as a row of matrices $\mathsf{K}^{(\mathrm{row})} = [\mathsf{K}_1, \ldots, \mathsf{K}_t, \ldots, \mathsf{K}_{|T|}]$ or as a column of matrices $\mathsf{K}^{(\mathrm{col})} = [\mathsf{K}_1; \ldots; \mathsf{K}_t; \ldots; \mathsf{K}_{|T|}]$ of M2L operators. The cardinality $|T|$ gives the number of transfer vectors in the interaction list T. Next, both big matrices are compressed using truncated singular value decompositions (SVD) of accuracy ε as

$$\mathsf{K}^{(\mathrm{row})} \sim \mathsf{U}\Sigma\mathsf{V}^* \quad \text{and} \quad \mathsf{K}^{(\mathrm{col})} \sim \mathsf{A}\Gamma\mathsf{B}^* \tag{17}$$

with the unitary matrices U, B of size $\ell \times r$ and V, A of size $|T|\ell^3 \times r$ and the r singular values in Σ, Γ. With a few algebraic transformations each M2L operator can be expressed as

$$\mathsf{K}_t \sim \mathsf{U}\mathsf{C}_t\mathsf{B}^* \quad \text{where} \quad \mathsf{C}_t = \mathsf{U}^*\mathsf{K}_t\mathsf{B} \quad \text{of size } r \times r \text{ is computed as} \quad \mathsf{C}_t = \Sigma\mathsf{V}_t^*\mathsf{B} \quad \text{or} \quad \mathsf{C}_t = \mathsf{U}^*\mathsf{A}_t\Gamma. \tag{18}$$

The advantage of this representation is that the cost of applying the M2L operator gets reduced from applying a matrix of size $\ell^3 \times \ell^3$ to a matrix of only $r \times r$. Moreover, less memory is required. However, the precomputation time grows cubically with the accuracy of the method due to the complexity of the SVD. In [12] the SVD has been substituted by the adaptive cross approximation (ACA) followed by a truncated SVD [1]. The precomputation time has been cut down drastically due to the linear complexity of the ACA.

4.1.1 SA with recompression (SArcmp)

If we use the SA variant the achieved low-rank r is the same for all M2L operators given by C_t. To a large extent, r is determined by the greatest individual low-rank of the M2L operators. This means that most of the matrices C_t of size $r \times r$ have effectively a smaller low-rank $r_t \leq r$. We exploit this fact by individually approximating them as

$$\mathsf{C}_t \sim \bar{\mathsf{U}}_t\bar{\mathsf{V}}_t^* \quad \text{with } \bar{\mathsf{U}}_t, \bar{\mathsf{V}}_t \text{ of size } r \times r_t \text{ and the constraint} \quad r_t < r/2. \tag{19}$$

Without the constraint the low-rank representation is less efficient than the original representation. The effects of the recompression are studied in Sec. 5.2.

4.2 Individual low-rank approximation (IA)

As opposed to the SA approach, an individual low-rank approximation of the M2L operators as

$$\mathsf{K}_t \sim \mathsf{U}_t\mathsf{V}_t^* \quad \text{with } \mathsf{U}_t\mathsf{V}_t \text{ of size } \ell^3 \times r_t \tag{20}$$

directly leads to the optimal low-rank representation of each of them. As in Sec. 4.1, the approximation can be performed by either a truncated SVD or the ACA followed by a truncated SVD (note, the rank r_t in the Eqn. (19) and (20) might be similar has not to be the same, though). This is also the case for the SArcmp variant, but it requires the approximation and storage of all M2L operators. In terms of time and memory however, it would be desirable to come up with a method that requires the approximation and the storage of a smaller number of operators only. Let us present a set of optimizations that fulfill these two requests.

4.2.1 Symmetries and permutations

Here, we illustrate how the full set of M2L operators can be expressed by a subset only. The idea is based on symmetries in the arrangement of M2L operators and exploits the uniform distribution of the interpolation points. We start by presenting the idea using a model example. After generalizing this idea, we demonstrate that M2L operators can be expressed as permutations of others.

Model example The target cell X in Fig. 1 has three interactions Y_t with the transfer vectors $t \in \{(2,1),(1,2),(-2,1)\}$. We choose the reference domain to be given by $t_1 \geq t_2 \geq 0$. The goal is to express the M2L operators of all interactions via M2L operators of interactions that lie in the reference domain only. In our example this is the interaction with the transfer vector $(2,1)$. The two transfer vectors $(1,2)$ and $(-2,1)$ can be shown to be reflections along the lines given by $t_1 = 0$ and $t_1 = t_2$, respectively. We easily find that any $t \in \mathbb{Z}^2$ can be expressed as a reflection (or a combination of reflections) of transfer vectors that satisfy $t_1 \geq t_2 \geq 0$.

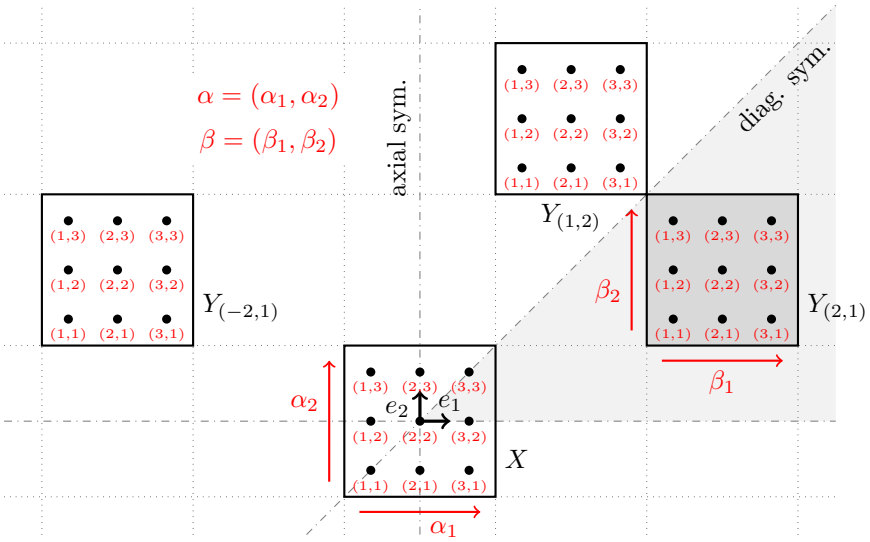

Figure 1: Axial and diagonal symmetries of interactions. The interpolation points $\bar{x}_\alpha$ and $\bar{y}_\beta$ are indexed by the multi-indices α and β, respectively (interpolation order $\ell = 3$). The only transfer vector that satisfies $t_1 \geq t_2 \geq 0$ is $t = (2,1)$. In that case, we claim that $\mathsf{K}_{(2,1)}$ is the only M2L operator we need to compute. The arrows indicate the construction of its multi-indices.

We claim that any reflection of a transfer vector corresponds to a permutation of the respective M2L operator. Recall that the evaluation of $K(\bar{x}_\alpha, \bar{y}_\beta)$ gives the entry from row $m(\alpha)$ and column $n(\beta)$ of the M2L operator. $\mathsf{K}_{(2,1)}$ is the only M2L operator whose transfer vector satisfies $t_1 \geq t_2 \geq 0$. The multi-indices are constructed as presented in Fig. 1. As can be checked, the entry $(\mathsf{K}_{(2,1)})_{mn}$ is not the same as $(\mathsf{K}_{(1,2)})_{mn}$ or $(\mathsf{K}_{(-2,1)})_{mn}$. However, if we use the permuted multi-indices from Fig. 2a for $\mathsf{K}_{(-2,1)}$ or those from Fig. 2b for $\mathsf{K}_{(1,2)}$ they are the same. The logic behind this can be summarized as follows.

- If an *axial symmetry* is given by $t_1 = 0$ as shown in Fig. 2a, we invert the corresponding component of the multi-index as
$$\alpha \leftarrow (\ell - (\alpha_1 - 1), \alpha_2) \quad \text{and} \quad \beta \leftarrow (\ell - (\beta_1 - 1), \beta_2). \tag{21}$$
- If the *diagonal symmetry* is given by $t_1 = t_2$ as shown in Fig. 2b, we swap the corresponding components as
$$\alpha \leftarrow (\alpha_2, \alpha_1) \quad \text{and} \quad \beta \leftarrow (\beta_2, \beta_1). \tag{22}$$

Sometimes it is necessary to combine axial and diagonal permutations. Take as example the transfer vector $(-1, 2)$: we need to flip it along $t_1 = 0$ and then along $t_1 = t_2$ to get $(2, 1)$. Note that reflections are non commutative, i.e., the order of their application matters. This is also true for permutations of the M2L operators.

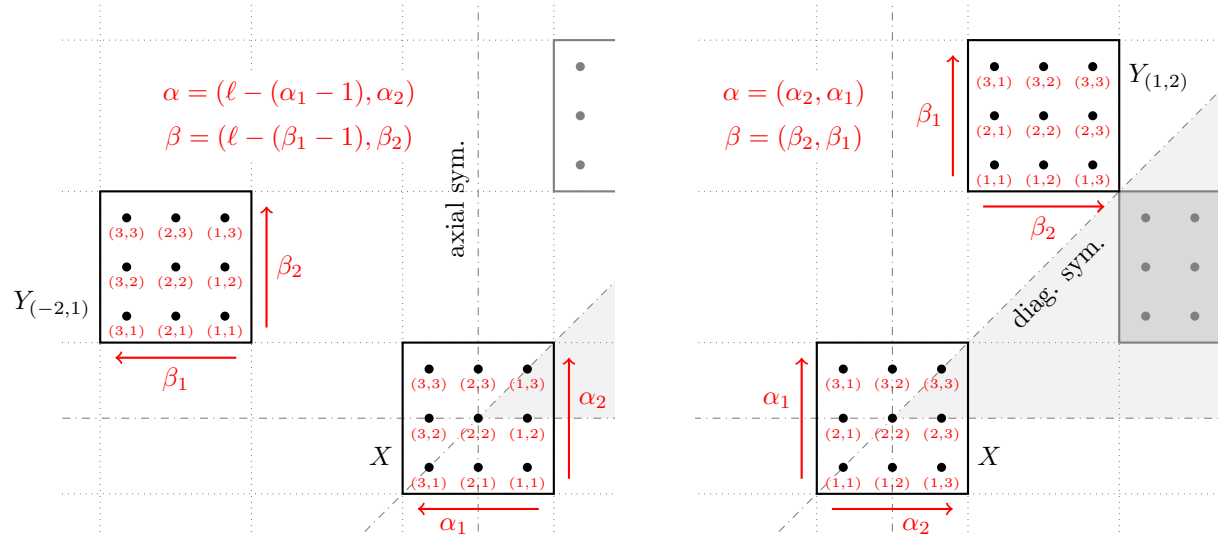

(a) Invert the component α_1 and β_1 due to the axial symmetry $t_1 = 0$.

(b) Swap the components $\alpha_1 \leftrightarrow \alpha_2$ and $\beta_1 \leftrightarrow \beta_2$ due to the diagonal symmetry $t_1 = t_2$.

Figure 2: The arrows indicate the construction of the multi-indices such that the M2L operators $\mathsf{K}_{(-2,1)}$ and $\mathsf{K}_{(1,2)}$ become the same as $\mathsf{K}_{(2,1)}$. In other words, the differences between these arrows and those from Fig. 1 determine the permutations of $\mathsf{K}_{(2,1)}$ such that it coincides with $\mathsf{K}_{(-2,1)}$ and $\mathsf{K}_{(1,2)}$.

Generalization Let us extend the above concept to the three dimensional case. We start by introducing three axial and three diagonal symmetries in $\mathbb{Z}^3$.

- *Axial symmetry planes* are given by $t_1 = 0$, $t_2 = 0$ and $t_3 = 0$ (see Fig. 3). Each of the three planes divides $\mathbb{Z}^3$ in two parts, i.e., the negative part $t_i < 0$ and the positive part $t_i \geq 0$. By combining all three planes $\mathbb{Z}^3$ is divided into octants. In the following we use $\mathbb{Z}^3_+$, i.e., the octant with $t_1, t_2, t_3 \geq 0$ as reference octant.
- *Diagonal symmetry planes* are given by $t_1 = t_2$, $t_1 = t_3$ and $t_2 = t_3$ (see Fig. 4). In $\mathbb{Z}^3$ there are six diagonal symmetries; however, we restrict ourselves to the symmetries affecting the reference octant $\mathbb{Z}^3_+$.

By combining the three diagonal symmetries and the three axial symmetries we obtain the cone shown in Fig. 5. We refer to it as $\mathbb{Z}^3_{\text{sym}}$; it is given by

$$\mathbb{Z}^3_{\text{sym}} = \{\mathbb{Z}^3_{\text{sym}} \subset \mathbb{Z}^3 : t_1 \geq t_2 \geq t_3 \geq 0 \text{ with } t \in \mathbb{Z}^3\}. \tag{23}$$

By its means we can identify the subset of transfer vectors $T_{\text{sym}} \subset T \subset \mathbb{Z}^3$ as

$$T_{\text{sym}} = T \cap \mathbb{Z}^3_{\text{sym}} \tag{24}$$

such that all others $T \backslash T_{\text{sym}}$ can be expressed as reflections of this fundamental set. Next, we claim that these symmetries are also useful for M2L operators.

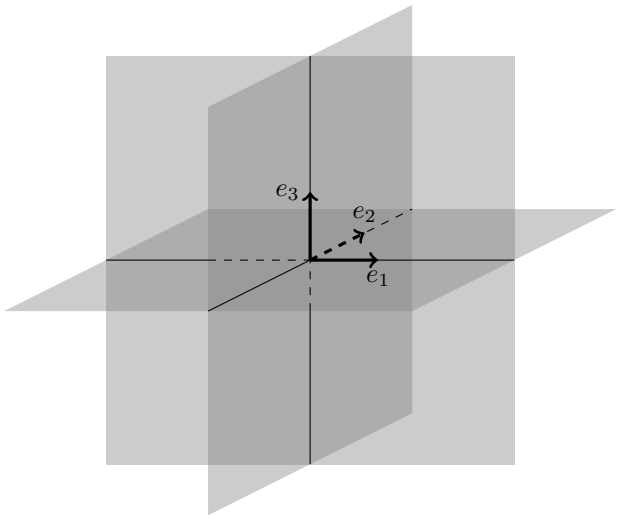

Figure 3: Three axial symmetry planes split $\mathbb{Z}^3$ in octants. The reference octant is given by $t_1, t_2, t_3 \geq 0$.

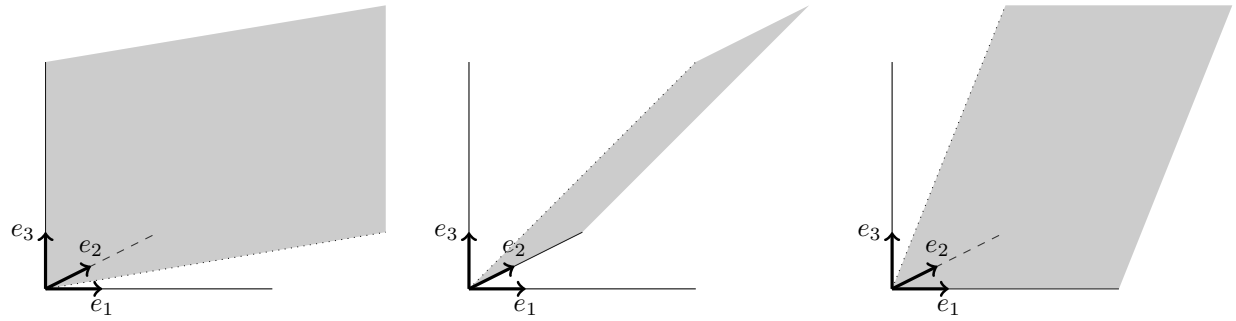

(a) $t_1 = t_2$ (b) $t_1 = t_3$ (c) $t_2 = t_3$

Figure 4: Three diagonal symmetry planes in the reference octant.

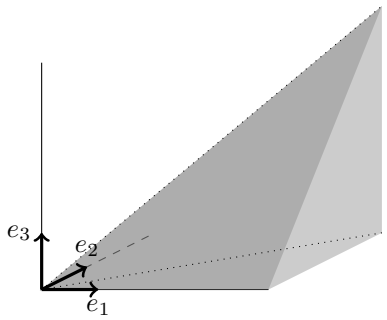

Figure 5: The final cone $\mathbb{Z}^3_{\text{sym}}$ ($t_1 \geq t_2 \geq t_3 \geq 0$) is obtained by combining axial and diagonal symmetries.

Permutation matrices Any reflection of a transfer vector determines the permutation of its associated M2L operator as

$$\mathsf{K}_t = \mathsf{P}_t \mathsf{K}_{p(t)} \mathsf{P}_t^\top. \tag{25}$$

The permutation matrix P_t depends on the transfer vector $t \in T$. We also need the surjective mapping $p : T \to T_{\text{sym}}$; it associates every transfer vector in T to exactly one in T_{sym}. The left application of P_t, essentially, corresponds to the permutation of α and its right application to the permutation of β, affecting rows (respectively columns) of the original matrix $\mathsf{K}_{p(t)}$. Note, the permutation matrices P_t depend only on the transfer vector t. How do we construct them? For some t we introduce axial and diagonal permutations π_t^{A} and π_t^{D} that read as follows.

- *Axial symmetries*: multi-index permutations are computed as

$$\pi_t^{\text{A}}(\alpha_1, \alpha_2, \alpha_3) = (\bar{\alpha}_1, \bar{\alpha}_2, \bar{\alpha}_3) \quad \text{with} \quad \bar{\alpha}_i = \begin{cases} \alpha_i & \text{if } t_i \geq 0, \\ \ell - (\alpha_i - 1) & \text{else.} \end{cases} \tag{26}$$

  There exist 8 different possibilities that correspond to the octants presented in Fig. 3. Note, $\pi_t^A(\alpha) = \alpha$ is only true for transfer vectors with $t_1, t_2, t_3 \geq 0$.

- *Diagonal symmetries*: multi-index permutations are computed as

$$\pi_t^{\text{D}}(\alpha_1, \alpha_2, \alpha_3) = (\alpha_i, \alpha_j, \alpha_k) \quad \text{such that} \quad |t_i| \geq |t_j| \geq |t_k|. \tag{27}$$

  There exist 6 different possibilities that correspond to the 6 different cones if we consider Fig. 5. Note again, $\pi_t^{\text{D}}(\alpha) = \alpha$ is only true for transfer vectors with $t_1 \geq t_2 \geq t_3 \geq 0$.

Given these multi-index permutations and the mapping functions $m(\alpha)$ and $n(\beta)$ we can define a permutation matrix P_t of size $\ell^3 \times \ell^3$. Its entries are 0 except in column j the entry $i = m(\pi_t(m^{-1}(j)))$ is 1. Let us go through the computation of this index: first, we compute the multi-index $\alpha = m^{-1}(j)$, then, we permute the multi-index $\bar{\alpha} = \pi_t(\alpha)$ and last, we compute the row-index $i = m(\bar{\alpha})$. Permutation matrices may be written as

$$\mathsf{P}_t = \left(e_{m(\pi_t(m^{-1}(0)))}, e_{m(\pi_t(m^{-1}(1)))}, \ldots, e_{m(\pi_t(m^{-1}((\ell-1)^3)))} \right), \tag{28}$$

where e_j denotes a column unit vector of length ℓ^3 with 1 in the jth position and 0 elsewhere. Permutation matrices are orthogonal $\mathsf{P}_t \mathsf{P}_t^\top = \mathsf{I}$, hence, the inverse exists and can be written as $\mathsf{P}_t^{-1} = \mathsf{P}_t^\top$. Note that the combination of permutations is non commutative. Given these permutations π_t^{A} and π_t^{D} we setup P_t^{A} and P_t^{D} and construct the permutation matrix as

$$\mathsf{P}_t = \mathsf{P}_t^{\text{D}} \, \mathsf{P}_t^{\text{A}}. \tag{29}$$

The permutation for the multi-index β is the same.

4.2.2 IA with symmetries (IAsym)

By exploiting the above introduced symmetries we end up with an optimization we refer to as the IAsym variant. We individually approximate and store only M2L operators with $t \in T_{\text{sym}}$ and express all others via permutations as shown Eqn. (25). The IAsym variant for an arbitrary transfer vector $t \in T$ consists of the following three steps.

1. Permute multipole expansions

$$\mathsf{w}_t = \mathsf{P}_t^\top \mathsf{w} \tag{30}$$

2. Compute permuted local expansions

$$\mathsf{f}_t = \mathsf{K}_{p(t)} \mathsf{w}_t \tag{31}$$

3. Un-permute local expansions

$$\mathsf{f} = \mathsf{P}_t \mathsf{f}_t \tag{32}$$

Note, the permutation matrix is not applied to the actual M2L operator (remains unchanged as can be seen in step 2). The application of a permutation matrix is implemented as a reordering of vector entries (step 1 and 3). Depending on whether the M2L operator exist in its full-rank or in its low-rank representation from Eqn. (20) the application corresponds to one or two matrix-vector products. In the following we introduce a blocking scheme that exploits the fact that many interactions share the same M2L operator. This leads to a faster execution on a computer.

4.2.3 IAsym with blocking (IAblk)

We know from Sec. 4.2.1 that if we consider symmetries and permutations, many interactions share the same M2L operators. This paves the road for blocking schemes. Essentially, their idea is to substitute many matrix-vector products by a few matrix-matrix products. Blocking schemes do not change the overall complexity of the algorithm, but they allow for the use of highly optimized matrix-matrix product implementations. They achieve much higher peak performances than optimized matrix-vector product implementations due to better cache reuse and less memory traffic [4, 9].

Algorithm 2 Blocking scheme with $|T_{\text{sym}}|$ matrix-matrix products

function BLOCKEDM2L(target cell X and all far-field interactions I_Y)
  allocate F_p and W_p for $p = 1, \ldots, |T|_{\text{sym}}$
  retrieve f from X
  set all $c_p = 0$
  for all source cells Y in I_Y **do**
    retrieve w from Y and compute t from cell-pair (X, Y)
    column $c_{p(t)}$ of $\mathsf{W}_{p(t)}$ gets $\mathsf{P}_t^\top \mathsf{w}$ ▷ Permute multipole expansions
    increment $c_{p(t)}$
  end for
  for all $\{\mathsf{K}_p\}$ **do**
    $\mathsf{F}_p \leftarrow \mathsf{K}_p \mathsf{W}_p$ ▷ Compute permuted local expansions
  end for
  set all $c_p = 0$
  for all source cells Y in I_Y **do**
    compute t from cell-pair (X, Y)
    retrieve f_t from column $c_{p(t)}$ of $\mathsf{F}_{p(t)}$
    increment $c_{p(t)}$
    $\mathsf{f} \leftarrow \mathsf{f} + \mathsf{P}_t \mathsf{f}_t$ ▷ Permute permuted local expansions
  end for
end function

In our concrete case we use it to block the multipole and local expansions. Instead of permuting them and applying the M2L operators individually (matrix-vector products), we assemble those that share the same M2L operator as distinct matrices and apply the M2L operators at once (matrix-matrix products). Algorithm 2 explains this in details. We need the matrices W_p and F_p of size $\ell^2 \times n_p$ for $p = 1, \ldots, |T_{\text{sym}}|$. Their columns store the permuted multipole and the resulting (also permuted) local expansions. The values for n_p indicate how many interactions in T share the same M2L operator of interactions in T_{sym}, in other words, $n_1 + \cdots + n_p + \cdots + n_{|T_{\text{sym}}|} = |T|$ is true. In the case of bbFMM this is a priori known, since the full interaction list is a priori given (see Sec. 3.2). That is not the case for dFMM and the values for n_p have to be determined during a precomputation step. We also need counters c_p to indicate the position of the currently processed expansions in W_p and F_p. As opposed to IAsym, here we split up the single loop over all interactions into three loops. In the first one, we assemble the set of matrices W_p. At the end $c_p \leq n_p$ is

true for all p. In the second loop, we perform at most $|T_{\text{sym}}|$ matrix-matrix products. And in the last loop, we increment the local expansion with the expansions from all F_p.

Blocking along multiple target cells Algorithm 2 proposes to use the blocking scheme for all interactions of only *one* target cell. In the worst case no M2L operator is shared and the algorithm coincides with IAsym. Moreover, the size of the matrices W_p and F_p might vary to a large extent. That is why we pursued the blocking idea further to come up with a more efficient scheme. Instead of using individual n_p we choose it to be a constant n for all $p = 1, \ldots, |T_{\text{sym}}|$. Then we keep on blocking expansions using interactions lists of *multiple* (as opposed to one) target cells. Once $c_p = n$ is true for some p, we apply the M2L operator as $\mathsf{F}_p = \mathsf{K}_p\mathsf{W}_p$ where $\mathsf{W}_p, \mathsf{F}_p$ are both of size $\ell^3 \times n$. In our numerical studies we use this blocking scheme with $n = 128$.

5 Numerical results

In the previous sections we introduced various optimizations of the M2L operators for bbFMM and dFMM. As representative kernel functions we use

$$\text{the Laplace kernel} \quad K(x,y) = \frac{1}{4\pi|x-y|} \quad \text{and the Helmholtz kernel} \quad K(x,y) = \frac{e^{\imath k|x-y|}}{4\pi|x-y|}. \tag{33}$$

In the numerical studies, hereafter, we use the same parameter setting as are used in the respective publications and for dFMM we use the wavenumber $k = 1$. All computations are performed on a single CPU of a Intel Core i7–2760QM CPU @ 2.40GHz × 8 with 8GB shared memory. We used the compiler gcc 4.6.3 with the flags "-O2 -ffast-math".

M2L optimizations We show and analyze results for the following eight variants:

1. NA: the full interaction list T is represented by full-rank (not approximated) M2L operators
2. NAsym: the reduced interaction list T_{sym} is represented by full-rank (not approximated) M2L operators
3. NAblk: same as NAsym but with additional blocking of multipole and local expansions
4. SA: the variant presented in [5] and briefly sketched in Sec. 4.1
5. SArcmp: same as SA but with additional recompression of all C_t
6. IA: same as NA but with low-rank (individually approximated) M2L operators
7. IAsym: same as NAsym but with low-rank (individually approximated) M2L operators
8. IAblk: same as NAblk but with low-rank (individually approximated) M2L operators (see Alg. 2)

Moreover, we study two different low-rank approximation schemes for the SA and IA variants: on one hand we use a truncated singular value decomposition (SVD) and on the other hand the adaptive cross approximation (ACA) followed by a truncated SVD [1].

Example geometries We use the three benchmark examples shown in Fig. 6 and described in the listing below. The depth of the octree is chosen such that near- and far-field are balanced, i.e., we want the fastest possible matrix-vector product.

1. The *sphere* from Fig. 6a is contained in the bounding-box $64 \times 64 \times 64$; 168 931 particles are randomly scattered on its surface. The octree has 6 levels.

2. The *oblate sphere* from Fig. 6b is contained in the bounding-box $6.4 \times 64 \times 64$; 125 931 particles are randomly scattered on its surface. The octree has 6 levels.

3. The *prolate sphere* from Fig. 6c is contained in the bounding-box $6.4 \times 6.4 \times 64$; 119 698 particles are randomly scattered on its surface. The octree has 7 levels.

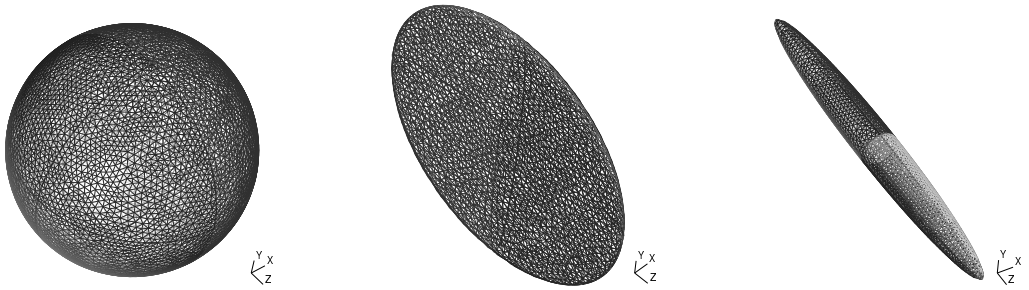

(a) sphere (b) oblate spheroid (c) prolate spheroid

Figure 6: The example geometries are centered at $(0, 0, 0)$

In approximative sense, the sphere is a three-dimensional, the oblate sphere a two-dimensional and the prolate sphere a one-dimensional object in $\mathbb{R}^3$. We choose these three geometries to study their influence on the performance on the dFMM. Table 2 shows the size of the full and the reduced interaction lists ($|T|$ and $|T_{\text{sym}}|$) per level (lf stands for low-frequency, hf for high-frequency regime) for all three geometries. The size of the interaction lists clearly grows with the dimensionality of the geometry. We report on the impact of this behavior later.

	sphere				oblate sphere				prolate sphere			
	3(hf)	4(hf)	5(hf)	6(hf)	3(hf)	4(hf)	5(hf)	6(hf)	4(hf)	5(hf)	6(hf)	7(lf)
$\lvert T\rvert$	668	18710	2666	418	60	2336	1502	400	214	738	382	424
$\lvert T_{\text{sym}}\rvert$	20	518	93	21	6	203	89	21	35	61	21	22

Table 2: Size of interactions lists per level for dFMM (hf and lf stands for high- and low-frequency regime, respectively)

5.1 Accuracy of the method

Both, the bbFMM and the dFMM, have two approximations: 1) the interpolation of the kernel functions determined by interpolation order ℓ, and 2) the subsequent low-rank approximation of the M2L operators determined by the target accuracy ε. The final relative error is a result of both approximations. We compute it as

$$\varepsilon_{L_2} = \left(\frac{\sum_{i \in M} |f_i - \bar{f}_i|^2}{\sum_{i \in M} |f_i|} \right)^{1/2} \tag{34}$$

where M is the number of particles x in an arbitrary reference cluster at the leaf level; f and $\bar{f}$ are the exact and approximate results, respectively. In Fig. 7 we compare achieved accuracies for the bbFMM and the dFMM with the IAblk variant (other variants produce identical results). Both plots show the behavior of the relative error ε_{L_2} depending on the interpolation order ℓ and the target accuracy ε. Evident is the matching result between the left and right figure. All curves show an initial plateau and then, after a sharp knee a slope of roughly 1. The knee occurs approximately at $(\ell, \varepsilon) = (Acc, 10^{-Acc})$. In the rest of the paper we use this convention to describe the accuracy Acc of bbFMM and dFMM. The low-rank approximations for the

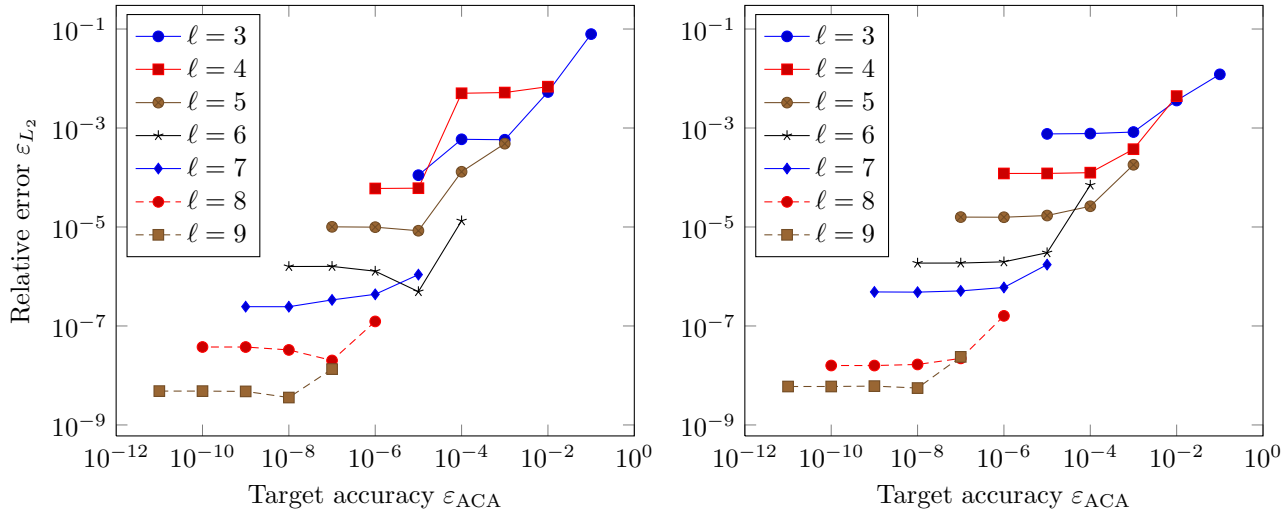

(a) bbFMM for the smooth kernel function

(b) dFMM for the oscillatory kernel function

Figure 7: Accuracies for the prolate sphere from Fig. 6c. The target accuracy ε_{ACA} refers to the accuracy of the approximate M2L operators (see Eqn. (20)). Here, we used the ACA followed by a truncated SVD.

computations whose accuracies are shown in Fig. 7 were conducted with the ACA followed by a truncated SVD. By just using a truncated SVD we obtain identical results.

5.2 Reducing the cost with the SArcmp variant

The cost of applying an approximate M2L operator mainly depends on its low-rank k. In Tab. 3 we compare the average rank of M2L operators for the SA and the IA variants at all levels that have expansions. Let us explain how we computed the average rank for the SA variant. Recall, when we use that variant, all M2L operators from one interaction list posses the same rank; the bbFMM and the dFMM in the low-frequency regime have one and the dFMM in the high-frequency regime has potentially multiple (directional) interaction lists per level. Thus, the average rank per level is computed as the average of all ranks used in all interactions at that level.

The application of one M2L operator from the SA variant requires $\mathcal{O}(k^2)$ and from the IA variant $\mathcal{O}(2k\ell^3)$ operations. Note, the ranks k of the M2L operators from the SA and the IA variants are different; normally, for a given accuracy Acc the rank for the IA variant is significantly lower than for the SA variant. This can be seen in Tab. 3. The large low-ranks at level 7 (first level in the low-frequency regime) of the SA variant are noteworthy. There, the lower bound for the separation criterion is given by the usual low-frequency criterion saying that non touching cells are admissible. Hence, the smallest possible transfer vectors have a length of $\min_{t \in T} |t| = 2$. The slowly decaying singular values of associated M2L operators are responsible for the large ranks. On the other hand, the upper bound for the separation criterion coincides with the lower bound of level 6 (parent level), which is in the high-frequency regime. Hence, the largest possible transfer vectors have a length of $\max_{t \in T} |t| \sim 4k$. M2L operators whose transfer vectors are in that range have much faster

	SA				IA			
Acc	4(hf)	5(hf)	6(hf)	7(lf)	4(hf)	5(hf)	6(hf)	7(lf)
3	9.8	12.3	12.8	19	5.4	5.7	5.7	5.0
5	21.7	30.8	39.2	71	11.3	12.3	13.5	12.6
7	38.2	58.6	80.0	163	18.9	21.5	24.7	24.1
9	57.8	96.5	138.7	296	28.6	33.2	39.7	40.1

Table 3: Comparison of average low-ranks k for the SA and IA variants of the dFMM (prolate sphere)

decaying singular values. This fact explains the efficiency of the SArcmp variant (individual recompression of each M2L operator).

In Tab. 4 we analyze the cost savings of the SArcmp variant compared to the SA variant. The left values in each column multiplied by 10^6 give the overall number of floating point operations per level for the SA variant. The right values (in brackets) indicate the respective cost ratio of the SArcmp versus the SA variant. The recompression reduces the cost remarkably (see also Fig. 8). At the low-frequency level 7, the SArcmp variant reduces the cost by more than a factor of 2. This is almost twice as much as in high frequency levels. For the impact on timing results we refer to Sec. 5.4.

	cost(SA)/10^6 (cost(SArcmp)/ cost(SA))							
Acc	4(hf)		5(hf)		6(hf)		7(lf)	
3	0.8	(0.98)	20.3	(0.93)	31.5	(0.93)	204.3	(0.62)
5	4.9	(0.97)	161.4	(0.89)	339.3	(0.86)	2889.3	(0.47)
7	19.3	(0.97)	687.8	(0.88)	1590.2	(0.83)	15420.0	(0.40)
9	55.0	(0.97)	2138.2	(0.87)	5237.6	(0.83)	51505.7	(0.38)

Table 4: Comparison of cost in terms of floating point operations for SA and SArcmp variants (prolate sphere)

In Fig. 8 we compare the cost of the SA, the SArcmp and the IA variants for bbFMM and dFMM for the prolate sphere and an accuracy $Acc = 9$. The bbFMM in Fig. 8a has expansions at the levels $2-7$. The reason for the jump between level 4 and 5 is because the levels $2-4$ have a maximum of $|T| = 16$ and the levels $5-7$ a maximum of $|T| = 316$ (common maximum size for bbFMM) possible M2L operators. The jump in the case of dFMM in Fig. 8b at level 5 can be explained in the same way: if we look at Tab. 2 we see that $|T|$ is about twice as large as it is at the other levels. The levels $4, 5, 6$ of dFMM are in the high-frequency regime. There the cost of the IA variant is approximately $12, 5, 3$ times greater than the cost of SA. However, at level 7 (low-frequency regime) of dFMM and at the levels $5-7$ of bbFMM the cost of the IA variant is only about 2/3 compared to the SA variant. The reason is the size of the interaction lists $|T|$. The larger they become the larger the span between smallest and largest low-rank and that favors individual approximations. The SArcmp is computationally the least expensive variant. Similar results are obtained for all other accuracies.

5.3 Speeding up the precomputation with IA variants

The bottleneck of the SA and SArcmp variants is the relatively large precomputation time. This is a minor issue in the case of homogeneous kernel functions. In that case the approximated M2L operators can be stored on the disk and loaded if needed for further computations. However, if we deal with non-homogeneous kernel functions, such as the Helmholtz kernel in Eqn. (33) the IAsym variant is the way to go. In Tab. 5 we compare the precomputation time of the SA, the IA and the IAsym variants (we do not report on the SArcmp variant; due to the additional recompression its precomputation time is higher than the one for the SA variant). For the low-rank approximation we use a truncated SVD or the ACA followed by a truncated

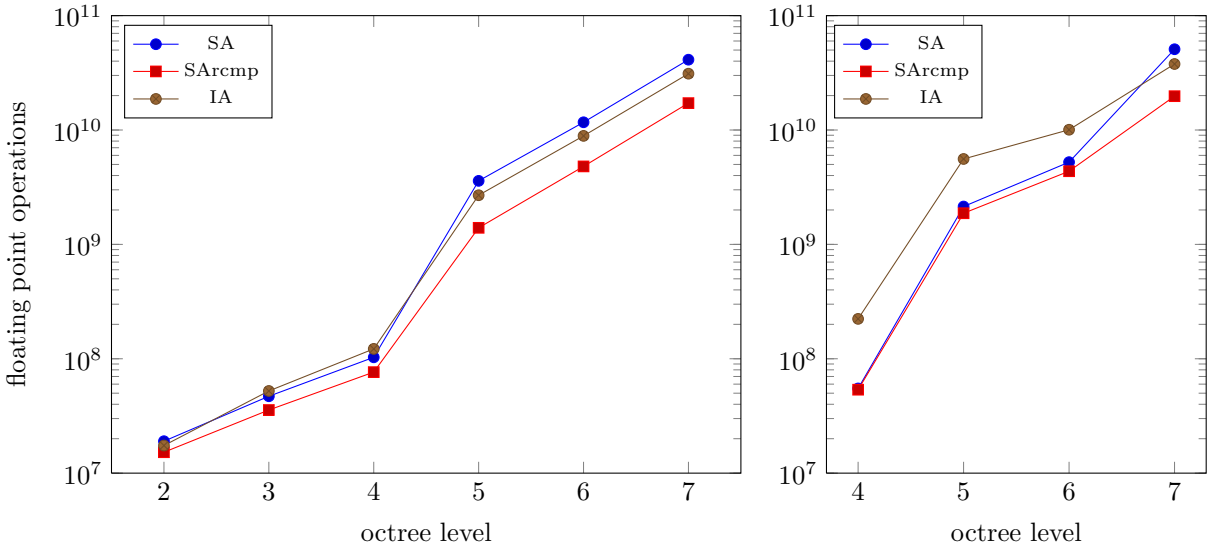

(a) bbFMM (b) dFMM

Figure 8: Comparison of the M2L cost (floating point operations) growth per level for the SA, SArcmp and IA variants of bbFMM and dFMM ($Acc = 9$ and prolate sphere)

SVD. In both cases we end up with the same low-rank. We get remarkable speedups in the precomputation. Let us look at an extreme example: for the sphere and an accuracy $Acc = 7$ we have $t_{\text{SVD}} = 4740.9\,\text{s}$ for the SA variant versus $t_{\text{ACA}} = 1.8\,\text{s}$ for the IAsym variant. This corresponds to a speedup of > 2600. For the oblate and prolate sphere we obtain similar results.

5.4 Comparison of all M2L variants

In the previous sections we have revealed the impact of the SArcmp and IAsym variants on the computational cost and the precomputation time of the M2L operators, respectively. In this section we compare all variants and focus on their impact on memory requirement and runtime. The tables 6, 7 and 8 (respectively, 9, 10 and 11) present absolute application times of the M2L operators for bbFMM (respectively, dFMM) and all three geometries. The upper set of rows reports on results obtained with a non optimized BLAS and Lapack implementation (libblas 1.2.20110419-2). The lower set shows the times obtained with the MKL [9], an optimized BLAS and Lapack implementation (Intel MKL 10.3.11.339 (intel64)).

Impact of using symmetries on the memory requirement Missing times in the tables indicate that the required memory exceeded the available memory of 8 GB. Clearly, the NA variant (no approximation nor use of symmetries) requires the most memory. On the other hand, IAsym and IAblk are the most memory friendly variants. Both require only memory for storing the low-rank representations of M2L operators from T_{sym} (see Tab. 2 for a comparison of T and T_{sym}).

Impact of the blocking scheme on runtime Bold numbers indicate the fastest variants. Two results attract our attention. 1) If we look at the times in the Tabs. 6 – 11 we notice that in four cases (bbFMM with the sphere, the oblate sphere and the prolate sphere and dFMM with the prolate sphere) IAblk, and in two cases (dFMM with the sphere and the oblate sphere) SArcmp is fastest. To be more general, IAblk wins at levels having non-directional expansions (all levels of bbFMM and low-frequency levels of dFMM) and SArcmp at levels having directional expansions (high-frequency levels of dFMM). Why is that? The

	SA		IA		IAsym	
Acc	t_{SVD} [s]	t_{ACA} [s]	t_{SVD} [s]	t_{ACA} [s]	t_{SVD} [s]	t_{ACA} [s]
sphere						
3	7.0	4.6	6.2	1.9	0.2	0.1
4	75.0	20.2	37.0	4.9	1.1	0.2
5	317.2	69.1	188.8	12.4	5.6	0.4
6	1336.4	197.0	790.5	28.6	22.9	0.9
7	4740.9	435.9	-	-	84.0	1.8
oblate sphere						
3	1.4	0.9	1.2	0.4	0.1	0.0
4	13.4	3.8	7.1	1.1	0.5	0.1
5	59.7	13.5	37.0	2.7	2.8	0.2
6	299.4	39.4	150.1	6.4	11.1	0.5
7	1021.2	97.6	551.0	13.3	40.9	0.9
8	-	217.7	1751.4	29.0	129.3	2.0
9	-	444.6	-	-	369.2	3.9
prolate sphere						
3	0.6	0.7	0.8	0.3	0.1	0.0
4	7.5	4.1	5.3	0.7	0.4	0.1
5	64.7	18.3	31.0	2.1	2.5	0.1
6	358.2	73,3	199.4	5.0	15.7	0.4
7	1374.8	204.3	808.9	11.6	66.0	0.8
8	-	549.3	-	25.0	322.3	1.7
9	-	1273.2	-	50.2	807.4	3.7

Table 5: Precomputation times (SVD versus ACA) for the SA, IA and IAsym variants. Missing numbers mean that the available memory of 8 GB has not been sufficient for the respective computation.

reason follows from the cost studies in Sec. 5.2. Let us take for example $Acc = 5$. Recall, we identify the computational cost with the size of the approximate M2L operators, ie., $\mathcal{O}(k^2)$ for SA and $\mathcal{O}(2k\ell^2)$ for IA. The respective ranks k are given in Tab. 3. The ratio of these costs for SA to IA is 0.46 at the high-frequency level 6 and 1.60 at the low-frequency level 7. As a matter of fact, at high-frequency levels wins the SA variant and at low-frequency levels the IA variant. Even savings of 47% at the low-frequency level due to the recompression of SArcmp (see Tab. 4) do not outweigh the advantage of the blocking scheme from IAblk. If there is no low-frequency level, such as for the sphere in Tab. 9 and the oblate sphere in Tab. 10, the SArcmp outperforms all other variants. For example, if we would repeat the computations for the prolate sphere with an octree of depth 6 (no low-frequency level) the resulting timing patterns would follow those from the sphere and the oblate sphere (the overall application time would increase too, since the tree-depth is based on our choice of balancing near- and far-field, i.e., the shortest overall application time). 2) Evident is the wide margin in the speedup of variants that use blocking and those which do not. If we use the MKL (as opposed to libblas) for the NA, NAsym, SA, SArcmp, IA and IAsym variants we end up with $1.5 - 2$ times faster application times. However, if we use the MKL for the NAblk and IAblk variants we achieve $3 - 4$ times faster times. Even though these speedups are greatest with the MKL library, it highlights the benefits of the blocking scheme presented in Alg. 2.

Varying growth of application times In Fig. 9 we visualize the different growth rates of M2L application times for the bbFMM with increasing accuracies *Acc*. We are interested in the growth rates due to algorithmic changes. That is why we only study those variants that do not use blocking. Since no approximation is

Acc	NA	NAsym	NAblk	SA	SArcmp	IA	IAsym	IAblk
libblas 1.2.20110419-2								
3	0.7	0.8	0.4	0.5	**0.3**	0.4	0.4	**0.3**
4	3.6	3.8	1.8	1.4	**0.9**	1.3	1.4	**0.7**
5	14.2	12.8	5.9	4.6	**2.2**	3.4	3.6	**1.8**
6	42.8	38.2	16.5	11.5	**4.8**	9.0	8.7	**4.2**
7	102.7	101.7	40.7	25.5	**9.6**	20.2	18.4	**8.6**
8	229.3	234.2	89.7	47.8	**18.3**	40.7	35.9	**16.2**
9	-	484.5	180.0	83.8	**30.0**	74.0	68.6	**28.4**
Intel MKL 10.3.11.339 (intel64)								
3	0.3	0.3	0.2	0.2	0.4	0.4	0.4	**0.2**
4	1.8	1.2	0.6	0.6	0.7	0.7	0.8	**0.4**
5	9.4	6.3	1.9	2.0	1.4	2.0	2.0	**1.0**
6	28.2	14.1	4.8	6.9	2.6	5.0	4.0	**1.7**
7	72.6	57.7	12.0	19.3	5.8	12.7	8.2	**3.5**
8	127.6	117.0	25.6	34.3	12.0	24.6	16.2	**6.0**
9	-	260.5	50.8	60.4	20.6	44.6	32.9	**9.9**

Table 6: M2L timings for the bbFMM (sphere)

Acc	NA	NAsym	NAblk	SA	SArcmp	IA	IAsym	IAblk
libblas 1.2.20110419-2								
3	0.3	0.4	0.2	0.2	**0.1**	0.2	0.2	**0.1**
4	1.6	1.6	0.8	0.8	**0.4**	0.6	0.6	**0.3**
5	6.4	5.8	2.6	1.9	**0.9**	1.6	1.6	**0.8**
6	19.1	16.7	7.4	5.4	**2.1**	4.0	3.9	**1.9**
7	46.8	44.8	18.3	11.2	**4.5**	9.0	9.0	**3.8**
8	102.8	101.9	40.1	21.3	**8.4**	18.2	16.5	**7.2**
9	-	212.2	81.1	37.0	**13.5**	32.4	30.4	**12.8**
Intel MKL 10.3.11.339 (intel64)								
3	0.1	0.1	0.1	0.1	0.2	0.2	0.2	**0.1**
4	0.7	0.5	0.3	0.3	0.3	0.3	0.4	**0.2**
5	4.5	2.0	0.9	1.0	0.7	0.9	0.9	**0.4**
6	13.1	6.7	2.2	3.2	1.2	2.6	1.8	**0.8**
7	33.7	27.4	5.4	8.2	2.7	5.7	4.4	**1.6**
8	57.9	52.7	11.5	14.6	5.2	10.9	7.2	**2.7**
9	117.4	118.2	22.9	27.3	9.1	20.0	14.2	**4.4**

Table 7: M2L timings for bbFMM (oblate sphere)

Acc	NA	NAsym	NAblk	SA	SArcmp	IA	IAsym	IAblk
libblas 1.2.20110419-2								
3	0.2	0.2	0.1	0.1	**0.1**	0.1	0.1	**0.1**
4	1.0	1.1	0.5	0.4	**0.3**	0.4	0.4	**0.2**
5	4.0	4.0	1.9	1.2	**0.6**	1.2	1.0	**0.6**
6	12.0	11.8	4.7	3.4	**1.3**	2.6	2.4	**1.4**
7	29.3	31.4	11.7	6.9	**2.8**	7.2	5.2	**2.9**
8	68.4	71.4	25.5	13.1	**5.2**	11.6	10.8	**4.9**
9	131.7	137.3	50.7	22.3	**8.6**	21.1	19.9	**8.7**
Intel MKL 10.3.11.339 (intel64)								
3	0.1	0.1	0.1	0.1	0.1	0.1	0.1	**0.1**
4	0.4	0.3	0.2	0.2	0.2	0.2	0.2	**0.1**
5	2.9	1.3	0.6	0.6	0.4	0.6	0.6	**0.3**
6	8.2	4.2	1.4	2.1	0.7	1.5	1.1	**0.5**
7	20.5	16.3	3.4	5.9	1.7	3.7	2.4	**1.0**
8	35.7	34.1	7.2	9.1	3.7	7.1	5.5	**1.7**
9	73.3	73.8	14.4	17.6	5.9	12.8	11.2	**2.8**

Table 8: M2L timings for bbFMM (prolate sphere)

Acc	NA	NAsym	NAblk	SA	SArcmp	IA	IAsym	IAblk
libblas 1.2.20110419-2								
3	6.3	5.9	4.8	2.0	**2.0**	3.2	2.9	3.5
4	25.7	25.1	20.1	4.3	**3.9**	8.0	8.1	8.3
5	113.0	89.5	71.4	7.4	**7.1**	19.8	19.4	19.7
6	-	275.9	202.2	14.5	**11.6**	43.0	42.8	40.4
7	-	-	-	-	-	-	86.5	78.1
Intel MKL 10.3.11.339 (intel64)								
3	4.8	3.9	2.3	1.6	**1.7**	3.2	2.4	2.2
4	21.5	17.1	7.5	3.3	**3.4**	6.7	5.9	4.8
5	109.1	61.5	22.8	6.3	**6.3**	10.6	14.0	10.0
6	-	162.2	58.8	11.6	**9.8**	35.1	29.7	17.6
7	-	-	-	-	-	-	60.8	30.8

Table 9: M2L timings for dFMM (sphere); high-frequency leaf level

Acc	NA	NAsym	NAblk	SA	SArcmp	IA	IAsym	IAblk
libblas 1.2.20110419-2								
3	1.8	1.8	1.6	0.6	**0.6**	0.9	0.9	1.1
4	8.9	8.6	6.8	1.3	**1.1**	2.7	2.6	2.7
5	31.4	30.6	24.8	2.8	**2.3**	6.9	6.8	6.9
6	91.8	95.9	71.6	5.5	**4.1**	15.9	15.9	14.8
7	-	228.4	176.6	9.6	**7.3**	32.1	32.3	28.9
8	-	-	-	16.4	**11.2**	59.2	59.6	52.7
9	-	-	-	25.5	**21.9**	-	105.1	90.1
Intel MKL 10.3.11.339 (intel64)								
3	1.4	1.0	0.7	0.4	**0.4**	0.7	0.8	0.6
4	7.2	5.0	2.4	0.9	**1.0**	2.0	1.8	1.3
5	25.8	20.7	7.9	2.2	**1.9**	5.5	4.5	3.1
6	62.5	56.7	20.4	4.3	**3.4**	12.6	10.3	5.9
7	-	141.3	48.8	7.8	**5.5**	24.7	21.8	11.0
8	-	-	-	13.6	**9.5**	45.3	42.0	18.8
9	-	-	-	21.0	**14.7**	-	79.6	30.9

Table 10: M2L timings for dFMM (oblate sphere); high-frequency leaf level

Acc	NA	NAsym	NAblk	SA	SArcmp	IA	IAsym	IAblk
libblas 1.2.20110419-2								
3	0.6	0.6	0.5	0.3	**0.2**	0.3	0.3	0.3
4	3.2	2.8	2.3	1.0	**0.5**	0.9	0.9	1.0
5	11.9	10.0	8.7	2.7	**1.2**	2.4	2.4	2.5
6	32.5	30.8	25.1	6.5	**2.6**	6.0	5.6	5.7
7	80.3	77.0	61.1	13.2	**5.1**	12.1	11.8	11.1
8	-	-	-	24.8	**9.1**	24.3	23.3	21.2
9	-	-	-	47.5	**18.6**	43.5	43.5	37.2
Intel MKL 10.3.11.339 (intel64)								
3	0.3	0.3	0.2	0.2	**0.2**	0.2	0.2	**0.2**
4	2.1	1.4	0.7	0.5	**0.4**	0.6	0.6	**0.4**
5	8.7	5.8	2.5	2.0	**1.0**	2.0	1.5	**1.0**
6	20.2	17.9	6.7	5.1	**2.0**	4.6	3.4	**2.0**
7	48.4	46.5	16.3	10.3	**4.0**	9.6	7.5	**3.8**
8	-	-	-	16.6	**7.2**	18.3	15.8	**7.0**
9	-	-	-	31.6	**14.8**	33.7	32.1	**11.6**

Table 11: M2L timings for dFMM (prolate sphere); low-frequency leaf level

involved the times for the NAsym variant grows the fastest. The times for the SA variant grow slower but still faster than those for the IAsym variant. The SArcmp variant features the slowest growth, it is the optimal variant in terms of computational cost (see Tab. 4).

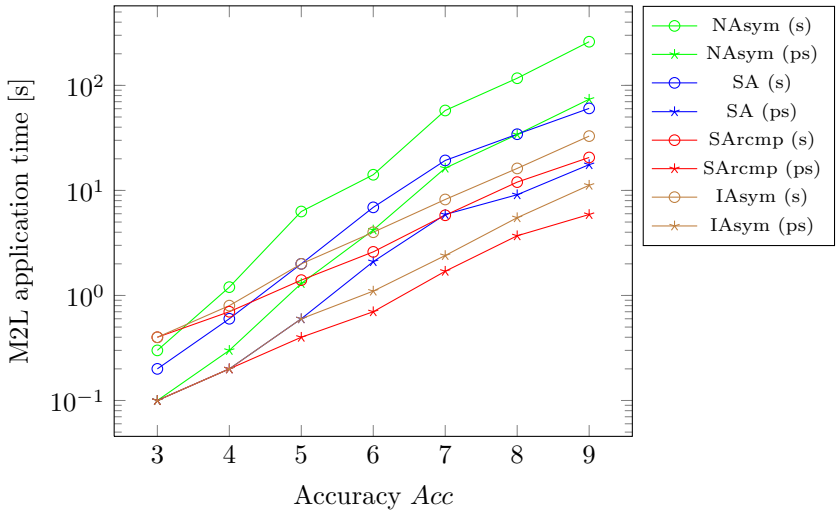

Figure 9: Running times versus accuracy for the NAsym, SA, SArcmp and IAsym variants for bbFMM taken from the Tabs. 6, 7 and 8; (s) stands for sphere and (ps) for prolate sphere

6 Conclusion

The fast multipole method based on Chebyshev interpolation, first presented in [5] for smooth kernel functions (bbFMM) and extended in [12] to oscillatory ones (dFMM), is a convenient-to-use algorithm due to its easy implementation and its kernel function independence. In this paper we investigated algorithms to reduce the runtime of the M2L operator. We proposed several optimizations and studied their respective strengths and weaknesses.

On one hand we proposed the SArcmp variant, which implies an individual recompression of the M2L operators obtained via SA, the variant presented in [5]. We have shown that this new variant reduces the computational cost noticeably. In some settings it even provides the fastest M2L application times. On the other hand we proposed a set of optimizations based on an individual low-rank approximation of the M2L operators; we refer to them as IA variants. As opposed to the SA variant they directly lead to the optimal low-rank representation of each operator, however, the overall cost is greater than for the SArcmp variant. The advantage of the individual treatment of the M2L operators is that we can exploit symmetries in their arrangement. This means that all operators can be expressed as permutations of a subset. For example, in the case of the bbFMM (constant size of the full interaction lists) we need to approximate and store only 16 instead of 316 operators. The remaining ones can be expressed as permutations thereof. This has a great impact on the precomputation time and the memory requirement. Moreover it allows to express (again in the case of the bbFMM) the at most 189 matrix-vector products (applications of the M2L operators) as at most 16 *matrix-matrix* products. We referred to this approach as the IAblk variant. It can then take advantage of highly optimized implementations of matrix-matrix operations (e.g., the MKL [9]).

Let us conclude by comparing SArcmp and IAblk, the two variants which have the fastest running times. IAblk wins if we compare precomputation time, required memory and runtime at levels having non-directional expansions (bbFMM and low-frequency levels in dFMM). SArcmp wins only if we compare the runtime at levels having directional expansions (high-frequency levels in dFMM). However, in order to identify the optimal variant we have to distinguish between two potential uses of the FMM as a numerical scheme to

perform fast matrix-vector products. 1) If we are interested in the result of a single matrix-vector product, a quick precomputation is essential, however, 2) if we are looking for the iterative solution of an equation system (many matrix-vector products), a fast M2L runtime is crucial. Let us explain this with a result. We take the dFMM (with MKL) of accuracy $Acc = 5$ for the sphere. The IAblk variant wins if we are interested in the former use. The precomputation takes 0.4 s versus 69.1 s and the M2L application takes 10.0 s versus 6.3 s which sums up to 10.4 s versus 75.4 s. All other operators (P2P, P2M, M2M, L2L and L2P) have nearly the same runtime. It is small compared to the one of the M2L operator and we disregard it. Looking at the latter use, the SArcmp variant starts being faster if the iterative solution requires more the 19 matrix-vector products. For higher accuracies this threshold rises, e.g., for $Acc = 6$ it lies at 26 matrix-vector products. If we take the bbFMM, the IAblk variant is optimal for both uses.

References

[1] M. Bebendorf. Hierarchical LU decomposition based preconditioners for BEM. *Computing*, 74:225–247, 2005.

[2] H. Cheng, W. Y. Crutchfield, Z. Gimbutas, L. Greengard, J. F. Ethridge, J. Huang, V. Rokhlin, N. Yarvin, and J. Zhao. A wideband fast multipole method for the Helmholtz equation in three dimensions. *Journal of Computational Physics*, 216(1):300–325, 2006.

[3] E. Darve and P. Havé. Efficient fast multipole method for low-frequency scattering. *Journal of Computational Physics*, 197(1):341–363, 2004.

[4] J. J. Dongarra, J. Du Croz, S. Hammarling, and I. S. Duff. A set of level 3 basic linear algebra subprograms. *ACM Trans. Math. Softw.*, 16(1):1–17, March 1990. ISSN 0098-3500. doi: 10.1145/77626.79170. URL `http://doi.acm.org/10.1145/77626.79170`.

[5] W. Fong and E. Darve. The black-box fast multipole method. *Journal of Computational Physics*, 228 (23):8712–8725, 2009.

[6] Z. Gimbutas and V. Rokhlin. A generalized fast multipole method for nonoscillatory kernels. *SIAM Journal on Scientific Computing*, 24(3):796–817, March 2002. ISSN 1064-8275.

[7] L. Greengard. *The rapid evaluation of potential fields in particle systems*. PhD thesis, Massachusetts Institute of Technology, 1987.

[8] L. Greengard and V. Rokhlin. A new version of the fast multipole method for the Laplace equation in three dimensions. *Acta Numerica*, 6:229–269, 1997.

[9] Intel®. Intel® Math Kernel Library (Intel® MKL) 10.3, 2012. URL `http://software.intel.com/en-us/articles/intel-mkl/`. [Online; accessed 28-August-2012].

[10] P. G. Martinsson and V. Rokhlin. An accelerated kernel-independent fast multipole method in one dimension. *SIAM Journal on Scientific Computing*, 29(3):1160–1178, May 2007. ISSN 1064-8275.

[11] J. C. Mason and D. C. Handscomb. *Chebyshev Polynomials*. Chapman & Hall/CRC, 2003.

[12] M. Messner, M. Schanz, and E. Darve. Fast directional multilevel summation for oscillatory kernels based on chebyshev interpolation. *Journal of Computational Physics*, 231(4):1175 – 1196, 2012.

[13] V. Rokhlin. Diagonal forms of translation operators for the Helmholtz equation in three dimensions. *Applied and Computational Harmonic Analysis*, 1:82–93, 1993.

[14] L. Ying, G. Biros, and D. Zorin. A kernel-independent adaptive fast multipole algorithm in two and three dimensions. *Journal of Computational Physics*, 196(2):591 – 626, 2004. ISSN 0021-9991.